Nanoscale

PAPER

View Article Online
View Journal | View Issue

Cite this: *Nanoscale*, 2015, **7**, 12133

Fabrication of SnO_2–SnO nanocomposites with p–n heterojunctions for the low-temperature sensing of NO_2 gas†

Lei Li,[a,b] Chunmei Zhang[a,c] and Wei Chen*[a]

Received 12th April 2015,
Accepted 3rd June 2015

DOI: 10.1039/c5nr02334c

www.rsc.org/nanoscale

In this report, the fabrication of a novel SnO_2–SnO nanostructure with p–n heterojunctions has been achieved through a facile one-pot and low-cost hydrothermal process. The structure and properties of the nanocomposite were analyzed with X-ray techniques and electron microscopy. HRTEM characterization showed that the p–n heterojunctions were formed with small n-type SnO_2 nanocrystals dispersed on the surface of large p-type SnO crystals. Compared to the single SnO_2-based material, a gas sensor fabricated from the SnO_2–SnO composite exhibited an enhanced sensing performance for NO_2 gas detection, with a limit of detection and sensitivity of 0.1 ppm and 0.26 ppm^{-1}, respectively, at a relatively low operating temperature (50 °C). Moreover, the p–n heterojunctions exhibited high sensing selectivity for NO_2. Such a high sensing sensitivity and a low operating temperature make the SnO_2–SnO p–n nanomaterial a promising gas sensor for practical NO_2 gas detection. The improved sensing response characteristics of the hybrid material could be attributed to the p–n junctions formed through the *in situ* growth of SnO_2 nanocrystals on SnO nanoplates. The present study is helpful for the design of novel gas sensing materials and the development of NO_2 gas sensors.

1. Introduction

Tin dioxide (SnO_2) nanomaterials have been widely applied in the field of gas sensing for decades due to their unique sensing properties, such as high sensitivity, fast response and high stability, *etc.*[1,2] Tin dioxide is a typical n-type semiconductor material with rutile crystalline structure and a wide band gap (3.6 eV). Many endeavors have been devoted to the design of SnO_2 nanostructures, and have resulted in many excellent achievements.[1,2] In particular, owing to their excellent tunable physicochemical properties and their size-, shape- and exposed surface-dependent gas sensing properties, SnO_2 nanomaterials with various structures have been designed for gas sensing, such as zero-dimensional (0D) particles[3,4] or clusters,[5] one-dimensional (1D) nanofibers[6,7] or nanorods,[8,9] two-dimensional (2D) nanosheets[10] and three-dimensional (3D) hierarchical and porous hollow structures,[11–14] *etc.* In order to overcome the intrinsic shortcomings of pure SnO_2 nanomaterials and to improve the sensing performance, many SnO_2 nanomaterials doped with different dopants have been proposed recently. Among the doped materials, the semiconductor materials doped or loaded with noble metals such as Pt,[15–18] Pd,[19–22] Au[23–25] and Ag[26,27] have been synthesized, and the doped SnO_2 materials exhibited enhanced sensing performances. However, due to the high cost and the easy poisoning of noble metals by toxic gases,[22,28,29] the application of noble metal-doped SnO_2 nanomaterials in gas sensors is largely limited. In recent years, it was found that hybrid sensing materials fabricated from different types of semiconductors by forming p–n heterojunctions with SnO_2 nanomaterials can effectively increase charge transfer and enhance the sensing properties.[30–33]

The unique heterojunction structure fabricated from SnO_2 and other doped or supported metal oxide materials with various morphologies has exhibited outstanding gas sensing properties. Compared with gas sensors based on a single SnO_2 material, nano-gas sensors fabricated from p–n heterojunction structures of SnO_2/metal oxides can largely overcome the shortcomings of high resistance, high working temperatures and long response times, *etc.*[30,33] In a p–n junction structure, between the contact sections of the n- and p-type semiconductor materials, the conduction and valence bands usually bend and the Fermi levels are equalized associated with the for-

[a]*State Key Laboratory of Electroanalytical Chemistry, Changchun Institute of Applied Chemistry, Chinese Academy of Sciences, Changchun 130022Jilin, People's Republic of China. E-mail: weichen@ciac.ac.cn; Tel: +86 431-85262723*
[b]*The College of Electrical and Electronic Engineering, Changchun University of Technology, Changchun 130012, People's Republic of China*
[c]*University of Chinese Academy of Sciences, Beijing 100039, People's Republic of China*

† Electronic supplementary information (ESI) available: Survey XPS spectrum of the SnO_2–SnO hybrid material. See DOI: 10.1039/c5nr02334c

mation of depletion layers, which directly results in the improvement of the conductivity and the acceleration of response and recovery times.[34,35] Moreover, the morphologies of metal oxides with hierarchical structures can be tuned to enhance the gas diffusion rate and enlarge the specific surface area, and thus to further improve the gas sensing properties. In recent years, typical SnO_2-based nanomaterials with p–n heterojunctions have been designed as gas sensors, *e.g.* SnO_2 nanoparticle-doped WO_3 nanolamellae for NO_2 sensing,[36] α-Fe_2O_3 nanorods grown epitaxially on the surface of SnO_2 nanosheets for acetone sensing,[37] heterostructured CuO nanoparticles and SnO_2 nanowires for H_2S detection,[34] ZnO/SnO_2 core–shell structural microspheres for ethanol sensing,[38] and so on. Meanwhile, heterostructures of SnO_2 metal oxide materials are not only confined to gas sensing applications, but also applied in electrochemical sensors,[39] photocatalysts,[40] lithium ion batteries,[41] dye-sensitized solar cells,[42] *etc*.

Nitrogen dioxide (NO_2) is a reddish-brown, high-activity gaseous substance, which is mainly released from high-temperature combustion processes, such as the exhaust gas emissions of automobiles, exhaust gas discharged from power stations and so on.[43,44] It is worth mentioning that NO_2 is also a key component of acid rain, which causes a variety of environmental effects, including visibility reduction in the atmosphere, surface water acidification and increased harmful toxins in fish and other aquatic organisms in water. Therefore, efficient sensing materials for the sensitive detection of NO_2 gas in the ambient with a fast response are essentially required.[45] In this paper, to develop practically useful NO_2 sensing materials, SnO_2–SnO hybrids with p–n junctions were fabricated through a one-step hydrothermal process. To the best of our knowledge, there is no previous report on the synthesis and NO_2 gas sensing properties of SnO_2–SnO hybrid materials with p–n junctions. The prepared SnO nanoplate–SnO_2 nanoparticle composites can effectively enhance the electron transfer and improve the response to the target NO_2 gas. The gas sensing tests showed that detection of NO_2 with a limit of detection of 0.1 ppm can be realized at a low temperature (50 °C) by using the prepared SnO_2–SnO p–n junctions as sensing probes. The present study demonstrates that designing novel semiconductor–semiconductor nanostructures with p–n heterojunctions is an efficient route to develop next-generation gas sensors with improved sensing performance.

2. Experimental section

2.1 Materials preparation

All reagents were of analytical grade and were used without further purification unless otherwise specified. The SnO_2–SnO nanocomposites were synthesized by a hydrothermal process. Typically, 0.066 g of $SnCl_2{\cdot}2H_2O$ (Beijing Chemical Reagent Co., Ltd, China, AR, 98%) and 0.054 g of urea were dissolved in 15 mL of deionized water under moderate stirring for about 30 min until the mixture appeared as a homogeneous milky solution. The mixed solution was then transferred to a 25 mL Teflon-lined stainless steel vessel and the hydrothermal process was performed at 180 °C for 16 h. The formed SnO_2–SnO composites were washed with water and ethanol by centrifugation (3000 rpm), and then dried at 40 °C for several hours in air to obtain the final product. In order to compare the gas sensing performances of the prepared SnO_2–SnO nanocomposites and single SnO_2 material, SnO_2 nanoparticles were also prepared by the same synthetic method and treatment procedure. In a typical synthesis, 0.105 g of $SnCl_4{\cdot}5H_2O$ (Chengdu Gracia Chemical Technology Co., Ltd, China, AR, 99%), and 0.054 g of urea were dispersed in 15 mL deionized water under magnetic stirring. Notably, this mixed solution was colorless and clear, which was different from that of $SnCl_2{\cdot}2H_2O$. The subsequent hydrothermal and purification processes were the same as that aforementioned.

2.2 Materials characterization

The composition and crystalline structures of the products were characterized by X-ray powder diffraction (XRD) on a Bruker D8 Advance X-ray diffractometer between 10° and 90° using a Cu Kα radiation source (λ = 1.54 Å). The morphologies and selected-area electron diffraction of the composites were characterized by transmission electron microscopy (TEM, JEOL 2000) and high resolution TEM (HRTEM, JEM-2010(HR) microscope). At the same time, the chemical states of the products were examined by X-ray photoelectron spectroscopy (XPS, VG Thermo ESCALAB 250 spectrometer). The Brunauer–Emmett–Teller (BET, Quantachrome Autosorb Automated Gas Sorption System) specific surface area and porosity properties analysis were also performed. UV-vis spectra were collected on a UV-3000PC Spectrophotometer (Shanghai Mapada Instruments Co., Ltd). Finally, the gas sensing properties of the materials were tested using a CGS-1TP (Chemical Gas Sensor-1 Temperature Pressure) intelligent gas sensing analysis system (Beijing Elite Tech Co., Ltd, China).

2.3 Gas sensing measurements

The gas sensing behavior of the samples was tested on a heating ceramic plate of the CGS-1TP instrument by pressing the sample firmly with two probes. The products were first mixed with *N*,*N*-dimethylformamide (DMF) to form homogeneous suspensions, which were then drip-dropped on commercial ceramic substrates with Ag–Pd interdigitated electrodes. The as-prepared samples were dried at 55 °C during the process of drip-dropping in air. The gas sensing measurements were conducted with the prepared sensors at different operating temperatures with a fixed working voltage of 9 V. The operating temperature was changed by an external temperature controller under the heating ceramic plate and could be adjusted from room temperature to 500 °C with a rate of 3–5 °C s^{-1} (the relative humidity was about 38%). The sensor was preheated for about 30 min at a certain target temperature until the resistance of the materials reached a stable range, and it was then sealed in an 18 L test chamber. The target gas was injected into the test chamber through the injection pore. During the measurements, the fans for gas

mixing were turned on until the resistance of the material reached a stable range. After the gas sensing tests, the test chamber was opened to expose the sensor to fresh air and the fans were turned off. These procedures were repeated for the gas sensing tests under different conditions. Here, the response of the sensor is defined as $R = R_g/R_a$, where R_g and R_a are the resistances of the sensor in the target gas and in air, respectively. The concentration of the target gas could be calculated using eqn (1):[43]

$$Q = V \times C \times 10^{-6} \times \frac{273 + T_R}{273 + T_B}, \quad (1)$$

where Q is the volume of the target gas, V is the volume of the test chamber, C is the concentration of the target gas, T_B is the operating temperature and T_R is the room temperature.

3. Results and discussion

3.1 Synthesis and characterization of the gas sensing materials

In this study, two kinds of NO_2 gas sensing materials (SnO_2–SnO nanocomposites and single SnO_2 nanoparticles) were prepared by one-pot hydrothermal processes. In the hydrothermal process, urea plays a key role for the formation of the SnO_2–SnO composites. When the temperature is higher than 90 °C, urea begins to hydrolyze and NH_4^+ and CO_3^{2-} are slowly released. With further increase in temperature, CO_2 and OH^- can be produced from CO_3^{2-} and NH_4^+, respectively.[46] Owing to the limited oxygen amount in the solution, only a small part of the SnO can be converted to SnO_2 to form the SnO_2–SnO composite. While totally oxygen-free conditions are hard to achieve in the hydrothermal process, pure SnO product cannot be prepared with the present method. The main reactions from the Sn^{2+} and Sn^{4+} precursors could be described as follows:

$$\text{I. } H_2NCONH_2 + 3H_2O \rightarrow 2NH_4^+ + CO_3^{2-} + OH^- + H^+ \quad (2)$$

$$\text{II } Sn^{2+} + 2OH^- \rightarrow Sn(OH)_2 \quad (3)$$

$$Sn(OH)_2 \rightarrow SnO + H_2O \quad (4)$$

$$2SnO + O_2 \rightarrow 2SnO_2 \quad (5)$$

$$\text{III } Sn^{4+} + 4OH^- \rightarrow Sn(OH)_4 \quad (6)$$

$$Sn(OH)_4 \rightarrow SnO_2 + 2H_2O. \quad (7)$$

The compositions and crystalline structures of the obtained products were first characterized by X-ray techniques and electron microscopy. As shown in Fig. 1A, the XRD pattern of the heterojunction-structured SnO_2–SnO composite agrees well with standard cassiterite (SnO_2, JCPDS card no. 41-1445) and romarchite (SnO, JCPDS card no. 06-0395). However, the product synthesized from $SnCl_4{\cdot}5H_2O$ shows only a cassiterite SnO_2 phase (JCPDS card no. 41-1445). It is noteworthy that, compared with the diffraction peaks of the pure SnO_2 sample, the intensity and full widths at half-maximum (FWHM) of the diffraction peaks from the SnO_2–SnO composite are much

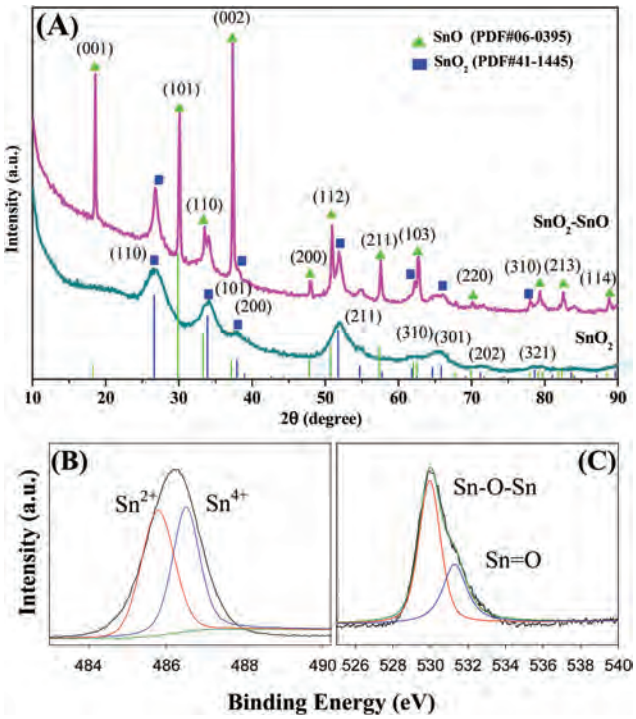

Fig. 1 (A) Typical XRD patterns of the SnO_2–SnO nanocomposite (purple) and SnO_2 nanoparticles (turquoise). For comparison, the XRD data of bulk SnO (green bars) and SnO_2 (blue bars) from the joint Committee Powder Diffraction Standard are also included. High resolution XPS spectra of Sn $3d_{5/2}$ (B) and O 1s (C) of the SnO_2–SnO nanocomposite.

stronger and narrower, respectively. These results imply that the SnO_2 nanocrystals formed in the SnO_2–SnO composite have higher degrees of crystallinity and relatively larger crystal sizes than the pure SnO_2 sample. On the other hand, such results suggest that during the formation of SnO_2–SnO hybrid materials, nucleation and crystal growth can be promoted. Interestingly, in the XRD pattern of SnO_2–SnO, the intensity and FWHM of the diffraction peaks from SnO are much stronger and narrower than those from the SnO_2 component, suggesting that the SnO nanocrystals are much larger than the SnO_2 nanoparticles. Meanwhile, from the standard XRD data of SnO (JCPDS card no. 06-0395), the (101) diffraction peak has the highest intensity ($I_{(001)}/I_{(101)}$ = 0.1, $I_{(002)}/I_{(101)}$ = 0.14). However, in the XRD pattern of the SnO_2–SnO composite, the (001) and (002) diffraction peaks are much stronger than the (101) peak, with the much increased $I_{(001)}/I_{(101)}$, $I_{(002)}/I_{(101)}$ ratios of 1.1 and 1.26. Such XRD features strongly suggest that the formed SnO nanocrystals in SnO_2–SnO are predominated by an exposed (001) facet. The lattice parameters of the (001), (101) and (002) facets were calculated to be c = 0.485, 0.485 and 0.436 nm, respectively, based on the MDI Jade 5.0 software. The crystallite sizes of SnO and SnO_2 in the SnO_2–SnO composite, and that of the pure SnO_2 nanoparticles, were evaluated to be 80.64, 28.4 and 4 nm, respectively, by the Scherrer equation: $d = 0.9\lambda/B_{2\theta}\cos\theta$ (λ: wavelength of the

X-rays; θ: angle of the peak; $B_{2\theta}$: the peak width at half-height), with the values of the FWHM of the major diffraction peaks of the SnO (002) and SnO_2 (110) planes. The calculated crystalline sizes are in accordance with the following results from the TEM and HRTEM measurements.

XPS measurements were also carried out to identify the chemical states of the SnO_2–SnO composite. Fig. S1† shows the full scale survey spectrum of the sample. Clearly, the peaks from Sn, O and C can be observed without the presence of any other impurities. From the high-resolution Sn $3d_{5/2}$ spectrum of the SnO_2–SnO composite shown in Fig. 1B, the two fitted peaks at 485.8 and 486.5 eV correspond to the Sn^{2+} and Sn^{4+} states, respectively.[30,47] Fig. 1C shows the high-resolution O 1s spectrum of the hybrid, in which the deconvoluted two peaks at binding energies of 529.9 and 531.2 eV correspond to the SnO_2 (Sn–O–Sn) and to the oxygen of SnO (Sn═O) bonds, respectively.[48] The XPS results are in good agreement with those of the XRD measurements. Both XRD and XPS characterization indicate that the SnO_2–SnO hybrid has been successfully fabricated through the hydrothermal process.

Fig. 2A and B show TEM images of the as-prepared pure SnO_2 nanoparticles at different magnifications. It can be seen that the obtained SnO_2 nanoparticles have tiny sizes. Due to the absence of any surfactants and supporting materials, the produced SnO_2 nanoparticles exhibit aggregates with a porous structure. Meanwhile, the SnO_2–SnO hybrids obtained by using different tin precursors through the same hydrothermal process exhibit a very different morphology from that of the pure SnO_2 material. Fig. 2C and D show TEM images of the SnO_2–SnO composite at different magnifications. It can be seen that in the composite, the SnO crystal exhibits a laminar structure of several hundreds and tens of nanometers in lateral size and thickness, respectively. At the same time, one layer of the SnO_2 nanoparticles of approximately 4–10 nm in diameter is dispersed on the surface of the large SnO plates, forming the heterojunction structures. To further examine the p–n heterojunction structure, a typical HRTEM image of the SnO_2–SnO hybrid is shown in Fig. 2E. Highly crystalline SnO_2 nanocrystals with clear lattice fringes from different facets can be observed. Meanwhile, the lattice fringes corresponding to the (001) plane of a SnO nanoplate can also be seen. A selected-area electron diffraction (SAED) pattern is shown in Fig. 2F. It can be seen that, in addition to the diffraction rings from multiple SnO_2 nanocrystals, there are also apparent diffraction spots, indicating the single crystalline phase of the SnO nanoplates. These electron microscopy analyses are in accordance with the above XRD and XPS measurements, showing the formation of SnO_2–SnO p–n structures with large SnO laminar crystals covered by small SnO_2 nanoparticles.

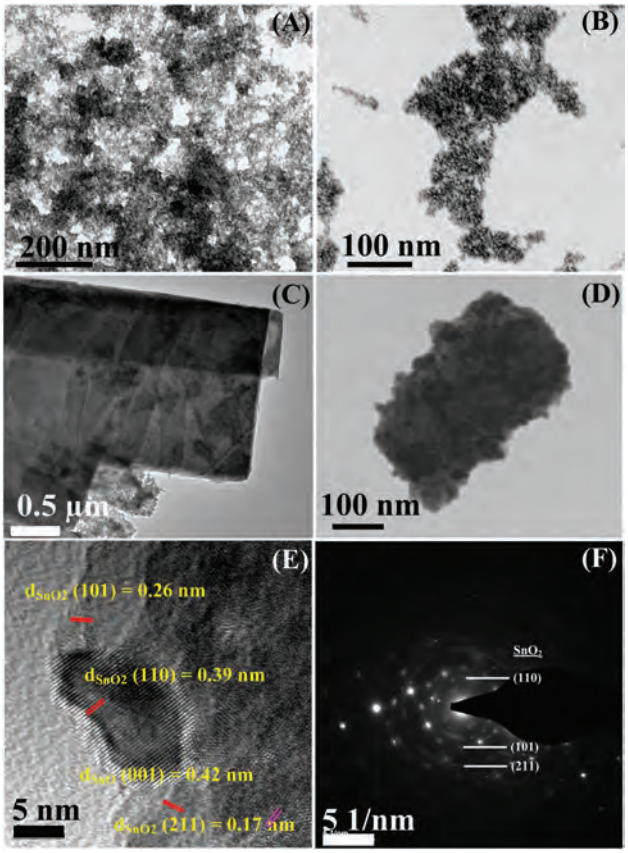

Fig. 2 (A, B) TEM images of the SnO_2 nanoparticles at different magnifications. (C, D) TEM images of the SnO_2–SnO hybrid at different magnifications. High-resolution TEM image (E) and a selected-area electron diffraction (SAED) pattern (F) of the SnO_2–SnO hybrid.

In order to quantitatively determine and compare the specific surface areas and pore volumes of the SnO_2 and SnO_2–SnO hybrid, multipoint BET surface area and pore volume measurements were carried out based on the nitrogen adsorption–desorption isotherms. The N_2 physisorption isotherms of the two samples and their corresponding Barrett–Joyner–Halenda (BJH) pore size distribution curves are shown in Fig. 3. One can see that the SnO_2–SnO hybrid exhibits an isotherm feature of the H3 type according to the IUPAC classification, whereas the pure SnO_2 sample shows a H2 type. From the measurements, the BET surface areas of SnO_2–SnO and SnO_2 are 45.6 and 178.9 $m^2\ g^{-1}$, respectively. As described above, the high surface area of the pure SnO_2 nanocrystals could be attributed to the small particle size and the porous structure which can be seen in the TEM characterization. On the basis of the BJH model and the desorption data, the average pore radii dV(d) of the SnO_2–SnO composite and SnO_2 nanoparticles were calculated to be 1.68 and 4.3 nm, respectively, as shown in the Fig. 3 insets.

3.2 Sensing performances of the SnO_2–SnO hybrid and pure SnO_2 nanoparticles for NO_2 gas detection

The sensing performances of the SnO_2–SnO hybrid and single SnO_2 for NO_2 gas detection were studied and compared. First, the operating temperature is one of the important sensing properties of materials, and a low operating temperature is especially favorable for their practical application in real gas sensors. Fig. 4 shows the responses of the two materials towards 50 ppm of NO_2 gas as a function of the operating temperature. It can be seen that for both materials, the

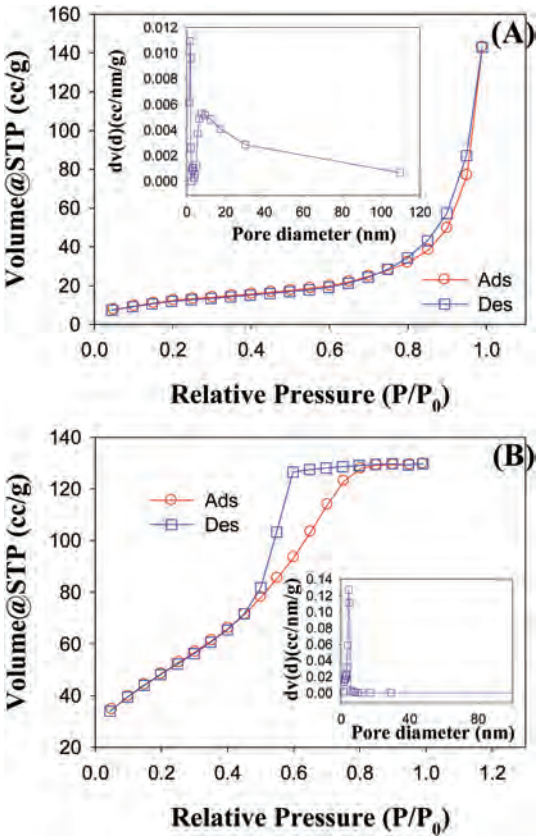

Fig. 3 N_2 adsorption–desorption isotherms of the SnO_2–SnO composite (A) and pure SnO_2 nanoparticles (B). The insets are the corresponding pore size distributions.

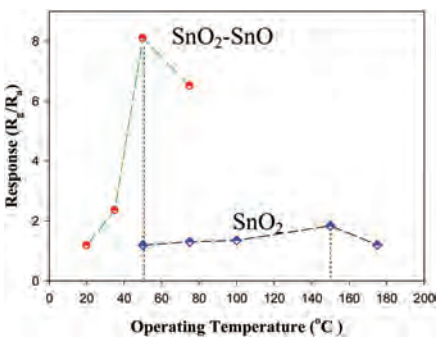

Fig. 4 Sensing responses of SnO_2–SnO and SnO_2 to 50 ppm NO_2 gas as a function of the operating temperature.

response intensity is dependent on the working temperature, *i.e.* increasing first with the appearance of a peak, and then declining with further increasing temperature . However, the response intensity and the optimum operating temperature are very different for the two materials. For the SnO_2–SnO hybrid, the sensing response gradually increases first with increasing temperature and reaches a maximum at 50 °C, and even at lower temperatures, *ca.* room temperature, the material still shows a relatively high response. Such a result implies that after further optimization, sensors based on the SnO_2–SnO hybrid could have the sensing ability for NO_2 gas detection at room temperature. This is a big breakthrough for semiconductor metal oxide-based gas sensors, since NO_2 gas sensing can be achieved at room temperature without any aid from noble metal doping or large surface-area supports (*e.g.* graphene, carbon nanotubes). However, the sensing response of the pure SnO_2 reaches a maximum at around 150 °C, which is triple that obtained from the SnO_2–SnO hybrid (50 °C). Moreover, the response intensity from pure SnO_2 is much lower than that from the SnO_2–SnO composite (about one fourth of that of the hybrid). From the XRD and TEM measurements, the particle size of pure SnO_2 is around 4 nm and the size of the SnO_2 nanoparticles on the surface of SnO is about 28 nm. According to the size effect, compared with larger nanoparticles, smaller-sized particles should have better sensing performances due to their larger surface area.[49] However, the present study shows that the SnO_2–SnO hybrid with larger particle size exhibits a much higher sensing performance. Therefore, the enhanced sensing performance of the SnO_2–SnO hybrid should be ascribed to the unique p–n heterojunction structure. Such excellent gas sensing properties with an enhanced sensing response and a much lowered operating temperature make the novel SnO_2–SnO hybrid structure a kind of promising gas sensor material for NO_2 gas detection.

The dynamic sensing response and recovery properties of the pure SnO_2 and SnO_2–SnO for NO_2 detection were investigated. Fig. 5A and B show the sensing responses of SnO_2 and SnO_2–SnO as a function of the concentration of NO_2 gas (from 15 to 110 ppm) at 150 and 50 °C, respectively. From Fig. 5A, it can be seen that with the increase in NO_2 concentration, the resistance of pure SnO_2 exhibits little change, indicating the non-sensitivity of pure SnO_2 even at high temperature (150 °C). However, as shown in Fig. 5B, at a much lower temperature (50 °C), the resistance of the SnO_2–SnO hybrid shows an increase with increasing NO_2 gas concentration. Moreover, the resistance could be almost completely recovered when the sensor was exposed to fresh air during the whole testing procedure. Such results indicate the high sensing sensitivity of the SnO_2–SnO hybrid toward NO_2 gas at a low temperature and suggest that the sensing mechanism of the SnO_2–SnO composites corresponds to that of typical n-type semiconductor metal oxides.

Interestingly, we also found that the pure SnO_2 exhibited different sensing characteristics at low and high temperatures. As shown in Fig. 5C, at 75 °C, the introduction of 50 ppm of NO_2 gas led to an increase in the resistance of the pure SnO_2. However, at 175 °C, the presence of NO_2 gas can result in a decrease in the resistance of SnO_2, which is totally opposite to the behavior at low temperature. In other words, pure SnO_2 exhibits n-type characteristics at low temperature (75 °C) but shows an overturned sensing behavior at 175 °C with a p-type sensing mechanism, which is different from those reported previously.[34,45] We will discuss this issue in the later section about the gas sensing mechanism. The responses of the SnO_2–

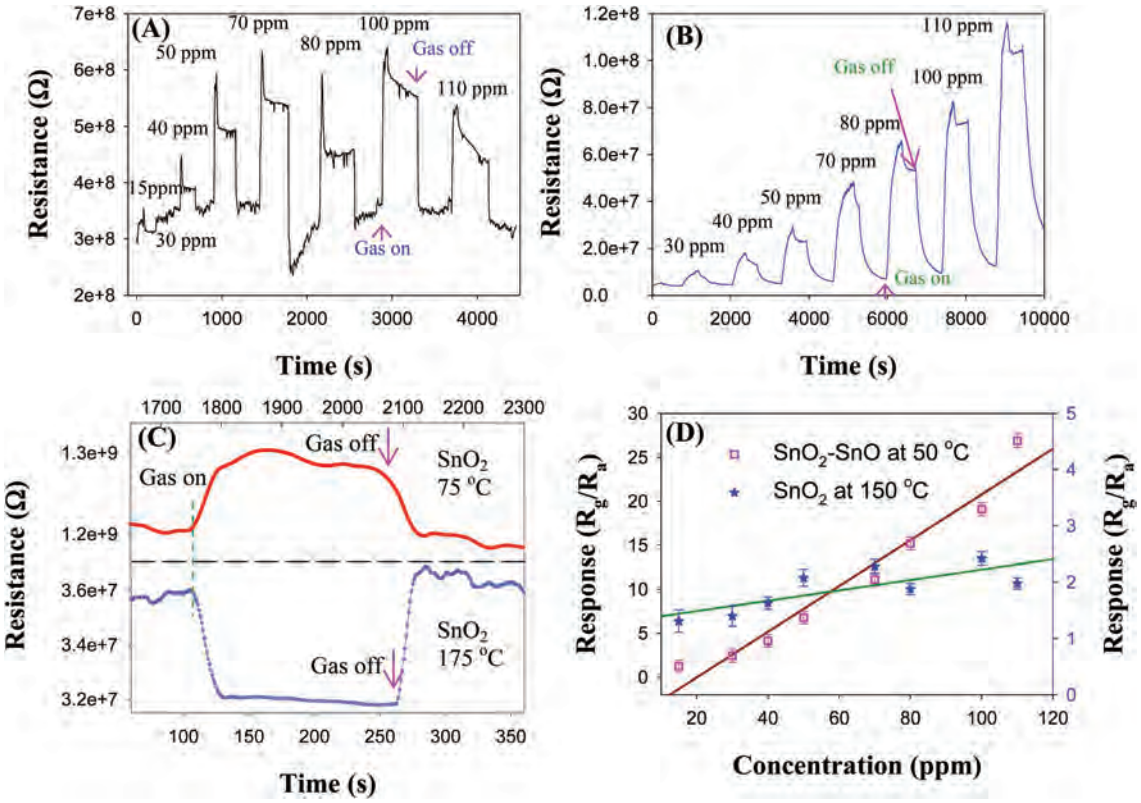

Fig. 5 Sensing responses of pure SnO_2 at 150 °C (A) and SnO_2–SnO at 50 °C (B) upon exposure to NO_2 gas with different concentrations varying from 15 to 110 ppm. (C) Sensing responses of pure SnO_2 to 50 ppm NO_2 gas at 75 °C (top) and 175 °C (bottom). (D) Response variations of SnO_2–SnO and SnO_2 as a function of NO_2 concentration at 50 and 150 °C, respectively. Solid lines show the linear fitting of the experimental data.

SnO hybrid and the pure SnO_2 as a function of NO_2 concentration are plotted in Fig. 5D. For the SnO_2–SnO hybrid in the whole concentration range, a good linear fit was obtained with R^2 = 0.943. From the slope of the calibration line, the sensitivity of the SnO_2–SnO hybrid for NO_2 detection was calculated to be 0.257 ppm^{-1}. Furthermore, the limit of detection (LOD) of the SnO_2–SnO hybrid was estimated to be 0.1 ppm based on the relation LOD = 3 α_D/α (where α is the slope of the linear part of the calibration curve and α_D is the standard deviation of the noise in the response curve in air).[50] In sharp contrast, a linear fit with R^2 = 0.555 was obtained from the pure SnO_2 nanoparticles. Compared with the high sensitivity and low LOD of the SnO_2–SnO hybrid, the pure SnO_2 material is not sensitive to the concentration variation of NO_2 gas (green fitting line) with sensitivity and theoretical LOD of 0.007 ppm^{-1} and 0.6 ppm, respectively. Meanwhile, it can be seen that the SnO_2 sensor reaches sensing saturation at a very low concentration, and thus the concentration change of the target gas can be hardly distinguished. These results strongly indicate that the SnO_2–SnO hybrid has an enhanced sensing performance for NO_2 gas compared to that of pure SnO_2 nanomaterials. Table 1 summarizes the sensing performances of SnO_2-based hybrid metal oxide nanomaterials with p–n heterostructures for the detection of different gases. Clearly, in this study, the optimum temperature, limit of detection and response intensity to 100 ppm target gas almost exceed those in the previous reports. The sensing selectivity of the SnO_2–SnO hybrid for NO_2 gas was also examined. As shown in Fig. 6, with SnO_2–SnO exposed to 100 ppm NO_2, C_2H_5OH and CO at 50 °C, the response intensity to NO_2 was significantly larger than those to C_2H_5OH and CO gases, indicating the high selectivity of the p–n heterojunction nanostructure for NO_2 detection. The significantly enhanced sensing performance of the SnO_2–SnO hybrid makes it a promising sensing material for applications in real NO_2 gas sensors.

3.3 Gas sensing mechanism of the SnO_2–SnO composite with p–n heterojunctions

From the above studies, the SnO_2–SnO hybrid with p–n junctions exhibited improved sensing properties compared to the pure SnO_2 material. Here, we propose a sensing mechanism of the SnO_2–SnO p–n heterojunction nanostructure. The semiconductive properties of the two materials were first studied.[51] Fig. 7 shows the variation of the resistances of the hybrid SnO_2–SnO and pure SnO_2 materials in air as a function of time in the temperature range from ~20 to 200 °C. We can see that these two sensing materials show different variation tendencies, although they belong to the same type of semiconductor metal oxides (n-type). SnO_2 is a well known n-type semiconductor (the majority of carriers are electrons). Thus,

Table 1 Summary of the gas sensing performances of SnO_2-based metal oxide nanomaterials with p–n heterostructures

Analyte gas	Composition	Synthesis route	Morphology	Opera. temp. (°C)	Response	Concentration	LOD	Ref.
NO_2	WO_3–SnO_2	Combinatorial solution deposition	SnO_2 particles loaded on WO_3 lamellae	200	N/A	200 ppb	N/A	36
C_2H_5OH	ZnO–SnO_2	Hydrothermal method	Core–shell	250	52.7	50 ppm	N/A	38
CH_3COCH_3	Fe_2O_3–SnO_2	Hydrothermal method	Core–shell	370	1.7	10 ppm	10 ppm	56
CH_3COCH_3	Fe_2O_3–SnO_2	Hydrothermal method	Fe_2O_3 nanorods grown on SnO_2 nanosheets	250	17	100 ppm	N/A	37
H_2S	CuO–SnO_2	Chemical vapour deposition	CuO particles onto SnO_2 nanowires	200	26.3	10 ppm	N/A	34
H_2S	CuO–SnO_2	Electrospun	Composite nanowires	300	650	100 ppm	N/A	31
$(CH_3)_2CHOH$	SnO_2–SnO_2	Chemical precipitation	Mixed phase SnO_2 nanorods	255	4.7	100 ppm	N/A	57
H_2	SnO_2–SnO	Hydrothermal method	SnO_2 particles loaded on SnO nanorods	120	N/A	N/A	N/A	30
NO_2	SnO_2–SnO	Hydrothermal method	SnO_2 nanoparticles loaded on SnO nanosheets	50	19.1	100 ppm	0.1 ppm	This work

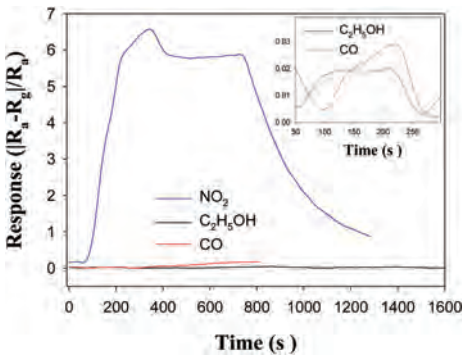

Fig. 6 Detection selectivity of the SnO_2–SnO hybrid for 100 ppm NO_2, C_2H_5OH and CO at 50 °C. The inset shows the magnified response curves for C_2H_5OH and CO.

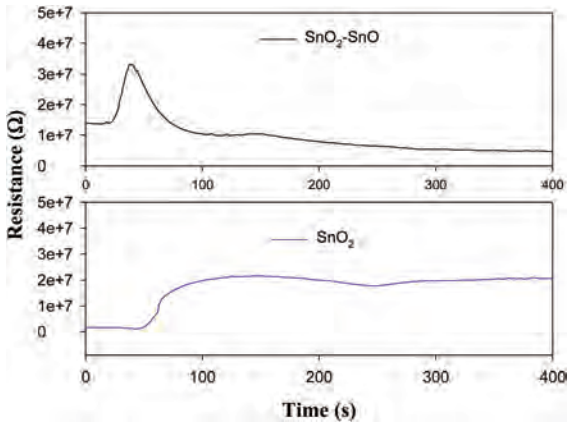

Fig. 7 Variation of the resistance (R_a) measured in air *versus* time for the SnO_2–SnO hybrid (top) and the SnO_2 (bottom), having varied temperature from approximately 20 to 200 °C (target temp.)

with rising temperature, the oxygen in air can be adsorbed on the surface of the SnO_2 to create chemisorbed oxygen species (O_2^-, O^-, O^{2-}) and consume the inner electrons. Such a process could produce surface polarization energy levels and result in the increase in the bulk resistance. With the oxygen species concentration reaching saturation, the bulk resistance enters a relative stable state (bottom of Fig. 7). As shown at the top of Fig. 7, the resistance variation of the SnO_2–SnO hybrid is a little more complicated than that of the pure SnO_2 sample. Compared with n-type SnO_2, SnO belongs to the p-type semiconductors (the majority of carriers are holes).[30,52] With increasing temperature, the resistance of the hybrid rises first and then declines to a stable state, which can be explained as follows: in the composite, oxygen is first adsorbed on the surface of the SnO_2 material and the oxygen ionization process can consume large amounts of free electrons, and thus holes are left in the composites, leading to the increase in the resistance just like for the pure SnO_2. With further increase in the temperature, the SnO nanocrystals become the active and main components for the chemisorption of oxygen, resulting in the further increase in hole concentration in the conduction band of the composite. The increase in hole concentration can enhance the speed of electron penetration on both sides of the p–n heterojunctions, resulting in the declining tendency of the resistance of the hybrids. Similar to that of the pure SnO_2 sample, the resistance reaches a relatively stable value in the end.

The n-type SnO_2 and p-type SnO can form a heterojunction structure at the interface, which is considered to be the primary reason for the enhanced sensing response and low operating temperature of the hybrid material.[53] As shown in Fig. 8A, theoretically, the forbidden band width between E_c (conduction band) and E_v (valence band) is 3.6 eV in a SnO_2 semiconductor and is about 2.9 eV in SnO. The p–n heterojunction leads to the formation of a depletion region. It can be seen that the bending of forbidden bands occurs at the interface zone to make the E_f (Fermi level) equilibrium between the

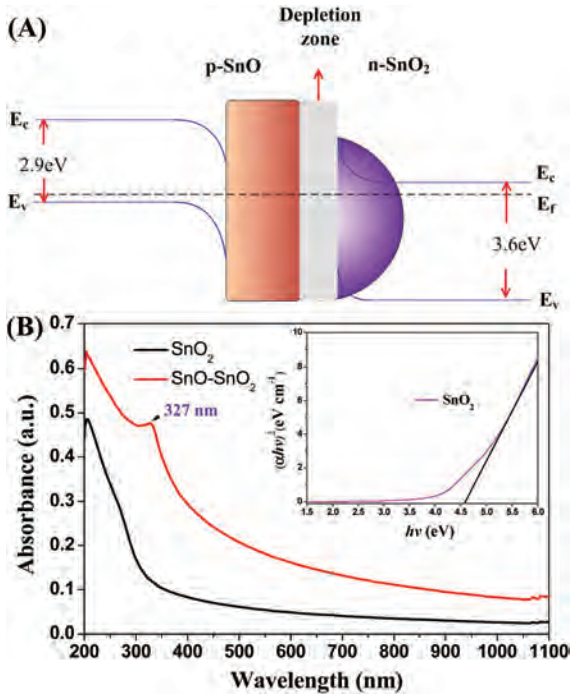

Fig. 8 (A) General schematic of the heterostructure of the n-SnO_2 nanoparticles on the surface of the p-SnO nanosheets with a p–n junction. (B) UV-vis spectra of the SnO_2–SnO and pure SnO_2 materials. The inset shows the plot of $(\alpha h\nu)^2$ *versus* $(h\nu)$ from the pure SnO_2).

SnO_2/SnO band gaps. In general, the narrower the width of the forbidden band, the lower the required energy for the transition of electrons near the bottom of the conduction band. UV-vis spectra of the SnO_2–SnO and pure SnO_2 materials are shown in Fig. 8B, from which the band gaps of these two samples can be evaluated. From the calculations, even though the actual forbidden band widths of these two samples are larger than that of bulk SnO_2 (3.6 eV) due to the quantum confinement effect, the band width of the SnO_2–SnO hybrid is much lower (3.79 eV) than that of the pure SnO_2 (4.6 eV). The change of the band gap can well explain the reason why the operating temperature of the SnO_2–SnO composite is much lower than that of the pure n-SnO_2. Meanwhile, as soon as the concentration of the oxygen anions (mainly O^-) gets to a saturation value, the height of the potential barrier and the width of the depletion region do not change.[54] The width of the depletion zone directly decides the response of a sensor at low temperature ranges. When the sensors are exposed to NO_2 gas (oxidizing gas), NO_2 molecules are absorbed on the surface of both SnO_2 and uncovered SnO. Similarly to the pure SnO_2 sensor, the absorbed NO_2 can capture the electrons from the conduction bands of the semiconductors, resulting in the increase in the resistance of the SnO_2–SnO composite which can be seen in Fig. 5B. After trapping electrons from the conduction band and oxygen anions, NO_2 gas molecules became NO_2^-. At the same time, the chemisorbed oxygen species were released in air once more. When the surface of the sample was almost fully covered by NO_2^-, the mobility of the free electrons on the surface was largely reduced, making the resistance of the composite increase to a saturation value. Meanwhile, the reduced mobility of the free electrons and the increased hole concentration could lead to the increase in the thickness of the depletion region, which may be another reason for the increase in sensor resistance.[47]

When NO_2 was adsorbed on the pure SnO_2, owing to the strong oxidability of NO_2, the electrons captured by NO_2 could be hardly exchanged with fresh oxygen, which may have been responsible for the poor recovery of the pure SnO_2. On the other hand, when the pure SnO_2 sensor was exposed to NO_2 gas at a high temperature, because of the high electron affinity, NO_3^- could be formed on the surface of the composites, and meanwhile, abundant holes were left in the conduction band and became the major carriers. Therefore, SnO_2 showed p-type semiconductor properties and the resistance showed a decrease in the process. Such an interesting phenomenon (called percolation behavior) has also been reported by Neri *et al.*[51,55]

4. Conclusions

The gas sensing properties of a SnO_2–SnO composite material with a p–n heterojunction structure have been investigated for the detection of NO_2 gas. The results showed that the sensing performance of the SnO_2–SnO hybrid is much higher than that of pure SnO_2 nanoparticles. The optimum temperature of the SnO_2–SnO sensor is as low as 50 °C, at which the sensor showed excellent linearity between the sensing response and the concentration of NO_2 gas, with a wide concentration range (15 to 110 ppm), low LOD (*ca.* 0.1 ppm) and good selectivity. Even though the pure SnO_2 nanoparticles possessed small crystalline grain sizes and large specific surface areas, the sensing performance of the pure SnO_2 for NO_2 gas detection was still lower than that of the SnO_2–SnO hybrids. In the proposed sensing mechanism, the p–n heterojunction structure formed at the interface of the SnO_2–SnO may account for the improved sensing performance, especially the much lowered operating temperature. The present study shows that, in addition to optimizing the crystal size and improving the specific surface area, fabricating semiconductor materials with a p–n heterojunction structure is also a very efficient way to design gas sensors with high sensing performances.

Acknowledgements

This work was supported by the National Natural Science Foundation of China (no. 21275136), the Natural Science Foundation of Jilin province, China (no. 201215090), Jilin province postdoctoral scientific research project (no. RB201317) and Jilin province education department scientific research project (no. 201592).

Notes and references

1 H. K. Wang and A. L. Rogach, *Chem. Mater.*, 2014, **26**, 123–133.
2 Z. W. Chen, D. Y. Pan, Z. Li, Z. Jiao, M. H. Wu, C. H. Shek, C. M. L. Wu and J. K. L. Lai, *Chem. Rev.*, 2014, **114**, 7442–7486.
3 M. D'Arienzo, D. Cristofori, R. Scotti and F. Morazzoni, *Chem. Mater.*, 2013, **25**, 3675–3686.
4 T. Kida, S. Fujiyama, K. Suematsu, M. Yuasa and K. Shimanoe, *J. Phys. Chem. C*, 2013, **117**, 17574–17582.
5 K. Suematsu, Y. Shin, Z. Q. Hua, K. Yoshida, M. Yuasa, T. Kida and K. Shimanoe, *ACS Appl. Mater. Interfaces*, 2014, **6**, 5319–5326.
6 X. L. Wang, N. Aroonyadet, Y. Z. Zhang, M. Meckenburg, X. Fang, H. T. Chen, E. Goo and C. W. Zhou, *Nano Lett.*, 2014, **14**, 3014–3022.
7 N. D. Chinh, N. V. Toan, V. V. Quang, N. V. Duy, N. D. Hoa and N. V. Hieu, *Sens. Actuators, B*, 2014, **201**, 7–12.
8 Y. J. Chen, L. Nie, X. Y. Xue, Y. G. Wang and T. H. Wang, *Appl. Phys. Lett.*, 2006, **88**, 083105.
9 Y. J. Chen, X. Y. Xue, Y. G. Wang and T. H. Wang, *Appl. Phys. Lett.*, 2005, **87**, 233503.
10 Z. Lou, L. L. Wang, R. Wang, T. Fei and T. Zhang, *Solid-State Electron.*, 2012, **76**, 91–94.
11 Y. Liu, Y. Jiao, Z. Zhang, F. Qu, A. Umar and X. Wu, *ACS Appl. Mater. Interfaces*, 2014, **6**, 2174–2184.
12 L. W. Wang, S. R. Wang, Y. S. Wang, H. X. Zhang, Y. F. Kang and W. P. Huang, *Sens. Actuators, B*, 2013, **188**, 85–93.
13 L. Mei, J. W. Deng, X. M. Yin, M. Zhang, Q. H. Li, E. D. Zhang, Z. Xu, L. B. Chen and T. H. Wang, *Sens. Actuators, B*, 2012, **166**, 7–11.
14 C. P. Gu, X. J. Xu, J. R. Huang, W. Z. Wang, Y. F. Sun and J. H. Liu, *Sens. Actuators, B*, 2012, **174**, 31–38.
15 A. V. Tadeev, G. Delabouglise and M. Labeau, *Thin Solid Films*, 1999, **337**, 163–165.
16 P. Ivanov, E. Llobet, X. Vilanova, J. Brezmes, J. Hubalek and X. Correig, *Sens. Actuators, B*, 2004, **99**, 201–206.
17 G. Neri, A. Bonavita, G. Micali, N. Donato, F. A. Deorsola, P. Mossino, I. Amato and B. De Benedetti, *Sens. Actuators, B*, 2006, **117**, 196–204.
18 X. Y. Xue, Z. H. Chen, C. H. Ma, L. L. Xing, Y. J. Chen, Y. G. Wang and T. H. Wang, *J. Phys. Chem. C*, 2010, **114**, 3968–3972.
19 Y. C. Lee, H. Huang, O. K. Tan and M. S. Tse, *Sens. Actuators,B*, 2008, **132**, 239–242.
20 T. Zhang, L. Liu, Q. Qi, S. C. Li and G. Y. Lu, *Sens. Actuators, B*, 2009, **139**, 287–291.
21 P. Sun, Y. S. Yu, J. Xu, Y. F. Sun, J. Ma and G. Y. Lu, *Sens. Actuators, B*, 2011, **160**, 244–250.
22 B. Kim, Y. J. Lu, A. Hannon, M. Meyyappan and J. Li, *Sens. Actuators, B*, 2013, **177**, 770–775.
23 C. Jin, H. Kim, S. Park, H. W. Kim, S. Lee and C. Lee, *Ceram. Int.*, 2012, **38**, 6585–6590.
24 F.-C. Chung, R.-J. Wu and F.-C. Cheng, *Sens. Actuators, B*, 2014, **190**, 1–7.
25 J. Zhang, X. H. Liu, S. H. Wu, M. J. Xu, X. Z. Guo and S. R. Wang, *J. Mater. Chem.*, 2010, **20**, 6453–6459.
26 S. W. Choi, A. Katoch, G. J. Sun, P. Wu and S. S. Kim, *J. Mater. Chem. C*, 2013, **1**, 2834–2841.
27 R.-J. Wu, D.-J. Lin, M.-R. Yu, M. H. Chen and H.-F. Lai, *Sens. Actuators, B*, 2013, **178**, 185–191.
28 M. M. Liu, R. Z. Zhang and W. Chen, *Chem. Rev.*, 2014, **114**, 5117–5160.
29 F. F. Ren, C. Q. Wang, C. Y. Zhai, F. X. Jiang, R. R. Yue, Y. K. Du, P. Yang and J. K. Xu, *J. Mater. Chem. A*, 2013, **1**, 7255–7261.
30 A. Shanmugasundaram, P. Basak, L. Satyanarayana and S. V. Manorama, *Sens. Actuators, B*, 2013, **185**, 265–273.
31 S. W. Choi, A. Katoch, J. Zhang and S. S. Kim, *Sens. Actuators, B*, 2013, **176**, 585–591.
32 M. Mashock, K. H. Yu, S. M. Cui, S. Mao, G. H. Lu and J. H. Chen, *ACS Appl. Mater. Interfaces*, 2012, **4**, 4192–4199.
33 N. D. Khoang, D. D. Trung, N. V. Duy, N. D. Hoa and N. V. Hieu, *Sens. Actuators, B*, 2012, **174**, 594–601.
34 F. Shao, M. W. G. Hoffmann, J. D. Prades, R. Zamani, J. Arbiol, J. R. Morante, E. Varechkina, M. Rumyantseva, A. Gaskov, I. Giebelhaus, T. Fischer, S. Mathur and F. Hernandez-Ramirez, *Sens. Actuators, B*, 2013, **181**, 130–135.
35 Z. J. Wang, Z. Y. Li, J. H. Sun, H. N. Zhang, W. Wang, W. Zheng and C. Wang, *J. Phys. Chem. C*, 2010, **114**, 6100–6105.
36 T. Kida, A. Nishiyama, Z. Hua, K. Suematsu, M. Yuasa and K. Shimanoe, *Langmuir*, 2014, **30**, 2571–2579.
37 P. Sun, Y. X. Cai, S. S. Du, X. M. Xu, L. You, J. Ma, F. M. Liu, X. S. Liang, Y. F. Sun and G. Y. Lu, *Sens. Actuators, B*, 2013, **182**, 336–343.
38 W. W. Guo, T. M. Liu, R. Sun, Y. Chen, W. Zeng and Z. C. Wang, *Mater. Lett.*, 2012, **89**, 5–8.
39 G. W. She, X. Huang, L. L. Jin, X. P. Qi, L. X. Mu and W. S. Shi, *Small*, 2014, **10**, 4685–4692.
40 K. T. Lee, C. H. Lin and S. Y. Lu, *J. Phys. Chem. C*, 2014, **118**, 14457–14463.
41 Y. Chen, J. Lu, S. Wen, L. Lu and J. M. Xue, *J. Mater. Chem. A*, 2014, **2**, 17857–17866.
42 S. H. Ahn, D. J. Kim, W. S. Chi and J. H. Kim, *Adv. Funct. Mater.*, 2014, **24**, 5037–5044.
43 L. Li, S. J. He, M. M. Liu, C. M. Zhang and W. Chen, *Anal. Chem.*, 2015, **87**, 1638–1645.
44 H. Zhang, J. C. Feng, T. Fei, S. Liu and T. Zhang, *Sens. Actuators, B*, 2014, **190**, 472–478.
45 A. Sharma, M. Tomar and V. Gupta, *Sens. Actuators, B*, 2013, **176**, 875–883.
46 H. J. Song, L. C. Zhang, C. L. He, Y. Qu, Y. F. Tian and Y. Lv, *J. Mater. Chem.*, 2011, **21**, 5972–5977.
47 F. Song, H. L. Su, J. J. Chen, W. J. Moon, W. M. Lau and D. Zhang, *J. Mater. Chem.*, 2012, **22**, 1121–1126.
48 H. L. Huang, Y. J. Liu, Q. Z. Gao, W. S. Ruan, X. M. Lin and X. Li, *ACS Appl. Mater. Interfaces*, 2014, **6**, 10258–10264.

49 C. N. Xu, J. Tamaki, N. Miura and N. Yamazoe, *Sens. Actuators, B*, 1991, **3**, 147–155.
50 R. K. Paul, S. Badhulika, N. M. Saucedo and A. Mulchandani, *Anal. Chem.*, 2012, **84**, 8171–8178.
51 G. Neri, S. G. Leonardi, M. Latino, N. Donato, S. Baek, D. E. Conte, P. A. Russo and N. Pinna, *Sens. Actuators, B*, 2013, **179**, 61–68.
52 A. K. Sinha, P. K. Manna, M. Pradhan, C. Mondal, S. M. Yusuf and T. Pal, *RSC Adv.*, 2014, **4**, 208–211.
53 X. H. Zhou, Q. X. Cao, H. Huang, P. Yang and Y. Hu, *Mater. Sci. Eng., B*, 2003, **99**, 44–47.
54 L. I. Trakhtenberg, G. N. Gerasimov, V. F. Gromov, T. V. Belysheva and O. J. Ilegbusi, *Sens. Actuators B*, 2012, **169**, 32–38.
55 N. Savage, B. Chwieroth, A. Ginwalla, B. R. Patton, S. A. Akbar and P. K. Dutta, *Sens. Actuators B*, 2001, **79**, 17–27.
56 S. F. Zhang, F. Ren, W. Wu, J. Zhou, X. H. Xiao, L. L. Sun, Y. Liu and C. Z. Jiang, *Phys. Chem. Chem. Phys.*, 2013, **15**, 8228–8236.
57 D. Hu, B. Q. Han, S. J. Deng, Z. P. Feng, Y. Wang, J. Popovic, M. Nuskol, Y. D. Wang and I. Djerdj, *J. Phys. Chem. C*, 2014, **118**, 9832–9840.